11th International Workshop on Ship and Marine Hydrodynamics
Hamburg, Germany, September 22-25, 2019

LES Study of Wind Turbine Wake Meandering in the Atmospheric Boundary Layer

Xu Ning, Yang Huang, Decheng Wan*

State Key Laboratory of Ocean Engineering, School of Naval Architecture, Ocean and Civil Engineering Shanghai Jiao Tong University, Collaborative Innovation Center for Advanced Ship and Deep-Sea Exploration, Shanghai, China

*Corresponding author: dcwan@sjtu.edu.cn

ABSTRACT

Actuator line model and CFD technique are introduced in the present work to learn the evolution of a wind turbine wake especially the wake meandering phenomenon under the atmospheric inflow condition. The simulation is implemented by applying the actuator line model to the ABL-LES solver, which is developed based on the CFD toolbox OpenFOAM by the researchers at the National Renewable Energy Laboratory (NREL). The time averaged velocity contours show that the shear layer starting behind the blade tip and root under turbulent inflow develops faster than that under uniform inflow, but under the strong mixing effect of atmospheric boundary flow the velocity inside the wake is redistributed immediately behind the rotor and the recovery process is much more accelerated than other cases. Temporal filter is used to smear out the high frequent turbulence while conserve the large scale flow structure. From the results of filtered flow field, it is found that uniform inflow and homogenous turbulent inflow cannot induce wake meandering and the large scale movement of wind turbine wake is only observed under atmospheric flow condition. Furthermore, a dominant wave length of $\lambda = 3.7D$ and a similar meandering frequency of $0.2 < St < 0.4$ in different positions downstream are obtained through further quantitative analysis.
Keywords: large eddy simulation, atmospheric boundary layer, actuator line model, wake meandering

1 INTRODUCTION

With the rapid development of the wind energy technology and the remarkable decline of the engineering cost, an increasing number of large wind farms containing tens of wind turbines are being built and put into use. To increase the total power generation and reduce structural loads of each wind turbine, a deep understanding of the formation and evolution of the wake of a wind turbine under different working regimes is necessary. Wake meandering, which is considered driven by the low frequent turbulence in the atmosphere[1], represents the large-scale movement of wind turbine wakes in both spatial and temporal dimension[2], dominating the aerodynamic characteristics of the entire far wake flow. Wake meandering usually accelerates the recovery procedure of the wake velocity deficit, but unfortunately it could also exacerbate the turbulent inflow of wind turbines located downstream, disturbing their power output and intensifying the fatigue loads[3, 19-22].

In order to identify the major factors that cause the meandering and how they affect the characteristics of the entire wake flow, plenty of experimental and numerical researches have been done. Medici and Alfredsson[4] observed the wake of a two-blade wind turbine model with and without freestream turbulence and detected a low-frequency fluctuation when the tip speed ratio was high. In their later study[5] the effect of the blade number, pitch angle and tip speed ratio on the wake meandering were discussed and they found the

Strouhal number ranged from 0.1~0.3 according to specific conditions. The study of Okulov and Sørensen[6] provided the theoretical basis for their experimental result and indicated the contribution of the periodically shed tip and root vortex to the unstable wake flow behavior. While Okulov et al.[7] detected in later experiments that the far wake oscillation in different operating conditions was subject to a constant Strouhal number of approximately 0.23, though the mutual interaction of vortex shed from blade tips and root dominated the near wake flow. Form the experiments in which a porous disc and a wind turbine model were successively introduced, Aubrun et al.[8, 9] found that the tip vortex and rotation of the wake induced by a rotating wind turbine became undiscernible form $3D$ (D represents the diameter of the rotor) downstream of the rotor and the wake meandering processes downstream of both the porous disk and the rotating turbine showed a high degree of similarity. By analyzing the velocity spectrum and the space-time correlations in the wake region under atmospheric boundary layer and homogeneous isotropic turbulent inflow, Espana et al.[10] concluded that the meandering phenomenon can only be attributed to the turbulent structure with a scale larger than the rotor diameter. Ivanell[11] investigated the relationship between the instability of the tip vortices behind the Tjaereborg wind turbine and the perturbation frequencies of the blade tips in favor of by introducing the actuator line model in large eddy simulation. Using the same method, Troldborg[12] simulated the wind turbine wake under both uniform and turbulent inflow and emphasized that the large scale structures of the ambient turbulence field governs the wake meandering. With the superiority of data acquiring in numerical simulation, Doubrawa[13] established the statistical methodology to identify the wake center and edge and tried to regenerate the synthetic wake for predictions of wind turbine loads and power.

This paper conducts the numerical simulations of a 5MW wind turbine represented by the actuator line model under the neutral atmospheric boundary layer. Focusing on the evolution of the wake, detailed wake information including velocity deficit, Reynolds stress and frequency spectrum is provided to study the main inducing factors and the intrinsic physical features of the wake meandering phenomenon.

2 NUMERICAL METHODS

2.1 Governing Equation

To achieve the information of the whole fluid field, the governing equation set consisting of the continuity equation and the momentum equation needs to be solved. Due to the unacceptable computational cost in the direct numerical simulation, large eddy simulation is implemented, which spatially filters out the small-scale flow and leads to the filtered governing equations as follows:

$$\frac{\partial \overline{u_i}}{\partial x_i} = 0 \tag{1}$$

$$\frac{\partial \overline{u_i}}{\partial t} + \frac{\partial}{\partial x_j}(\overline{u_j}\,\overline{u_i}) = -\underbrace{2\varepsilon_{i3k}\Omega_3\overline{u_k}}_{\text{I}} - \underbrace{\frac{\partial \tilde{p}}{\partial x_i}}_{\text{II}} - \underbrace{\frac{1}{\rho}\frac{\partial}{\partial x_i}p_0(x,y)}_{\text{III}} - \underbrace{\frac{\partial \tau_{ij}^D}{\partial x_j}}_{\text{IV}} + \underbrace{g(\frac{\overline{\theta}-\theta_0}{\theta_0})\delta_{i3}}_{\text{V}} + \underbrace{\frac{1}{\rho}f_i}_{\text{VI}} \tag{2}$$

Term I represents the Coriolis force caused by the earth rotation, where ε_{i3k} is the alternating tensor and Ω_3 is rotation rate vector. Term II is the gradient of pressure $\hat{p} = \overline{p} - p_0(x,y) + \rho_0 gz$ normalized by constant fluid density ρ and the one third of the stress tensor trace τ_{kk}. Term III is the background pressure gradient which drives the flow field to the specific state. In term IV, $\tau_{ij}^D = \tau_{ij} - \delta_{ij}\tau_{kk}/3$, τ_{ij} is the fluid stress tensor (consisting of both viscous and subfilter-scaled part) and δ_{ij} is the Kronecker delta. This term is computed in LES as:

$$\tau_{ij}^D = -2\upsilon^{SFS}\overline{S_{ij}} \tag{3}$$

where the SFS viscosity υ^{SFS} is modeled by the Smargorinsky model[14] and

$$\overline{S_{ij}} = \frac{1}{2}(\frac{\partial \overline{u_i}}{\partial x_j} + \frac{\partial \overline{u_j}}{\partial x_i}) \tag{4}$$

Term V models the buoyancy effects with $\bar{\theta}$ and θ_0 representing potential temperature and the reference temperature respectively. Term VI represents the body force generated by the wind turbine blades. The potential temperature appearing in term V is acquired by solving the temperature transport equation below:

$$\frac{\partial \bar{\theta}}{\partial t} + \frac{\partial}{\partial x_j}(u_j \bar{\theta}) = -\frac{\partial q_j}{\partial x_j} \tag{5}$$

$$q_j = -\frac{\upsilon^{SFS}}{\mathrm{Pr}_t}\frac{\partial \bar{\theta}}{\partial x_j} \tag{6}$$

Where q_j represents the temperature source item caused by molecular and SFS effects, with the turbulent Prandtl number Pr_t equal to 1/3.

Because the LES of high Reynolds-number wall-bounded turbulence requires quite high resolution and quality of the grids, a wall model developed by Moeng[17] is introduced to estimate the surface stress and thus avoid the unacceptable computational cost in the near-ground region. Given roughness length z_0, average surface temperature flux q_s and friction velocity u_* as input, this model computes the stress components τ_{13}, τ_{23} and the fluctuating temperature flux q_3 at ground level. z_0, q_s are directly prescribed to 0.15m, $0.00\mathrm{K}\cdot\mathrm{m/s}$ respectively and u_* is obtained through the Monin–Obukhov similarity theory[18].

2.2 Actuator Line Model

Instead of building a real physic model of the wind turbine, the actuator line model, firstly proposed by Sørensen and Shen[15], divides the blade into tens of segments and represents each segment by body force computed according to its attack angle and the local flow field. The body force is expressed as:

$$f = \frac{1}{2}\rho V_{rel}^2 c\left(C_l \overrightarrow{e_L} + C_d \overrightarrow{e_D}\right) \tag{7}$$

Where V_{rel} is the relative velocity experienced by the actuator point, c and is the cord length. C_l and C_d are the lift and drag coefficient, whose values are related to the local attack angle.

Directly acting the body force to isolated points in the flow field will cause numerical errors, so it is necessary to smoothly project the body force to a sphere region by the following formula:

$$f_\varepsilon = f \otimes \eta_\varepsilon \quad , \quad \eta_\varepsilon(d) = \frac{1}{\varepsilon^2 \pi^{3/2}} \exp\left[-\left(\frac{d}{\varepsilon}\right)^2\right] \tag{8}$$

Where $\otimes$ is convolution operator, and the regularization kernel η_ε is parameterized with d, the distance between the grid points and the actuator points, and ε, which controls the size of projection region.

3 SIMULATION SETUP

3.1 Domain Dimension

There are two main considerations when setting the main dimension of the computational domain. 1) The length needs to be large enough to simulate the flow in far wake region. 2) The scale of width and height should be the same as those of the possible large turbulent structures in the atmosphere, which could reach a thousand meters or more. Therefore, considering the above requirements and the limited computation resources, the length, width and height are set to 2016m, 800m and 800m respectively, i.e. a domain of $16D \times 6.35D \times 6.35D$ ($D = 126$ m is the rotor diameter of the wind turbine used in the simulation). To avoid the unphysical influence of the inlet boundary and the side planes, the wind turbine represented by the

actuator line model is placed in the central axis of the domain and $3D$ away from the inlet plane. The main dimensions and the case setup parameters are also indicated in Figure 1.

As seen in Figure 1, the computational domain is divided into three region with different mesh resolutions. The coarsest region I, where the side length of a mesh cell is 8m, is the background mesh. It should be mentioned that the near-wall region flow is not directly resolved in the present work but estimated by the wall-stress model, so the requirement for the mesh is that the first cell away from the ground should be within the theoretical logarithmic-law layer (Prandtl layer for ABL), of which the height is much larger than the size of our background mesh unit. The unit grid scale in region II is 4m so that the multi-scale vortex structures that dominates the movements of turbine wake could be well captured. Just enough to encompass the wind turbine, region III has the finest mesh resolution where the side length of a cell is up to 2m. Thus the total mesh number of the domain is 10 million and the generated computational mesh is showed in Figure 2. According to the mesh resolution of region III, the parameter ε should be twice the length of the mesh cell, thus set to 4. Besides, given the turbine rotating with the rated rotation speed $\Omega = 12.1$ rpm, time step $\Delta t = 0.02$ is decided following the principle that the path taken by the blade tip of the wind turbine in a time step should not exceed the side length of a mesh cell.

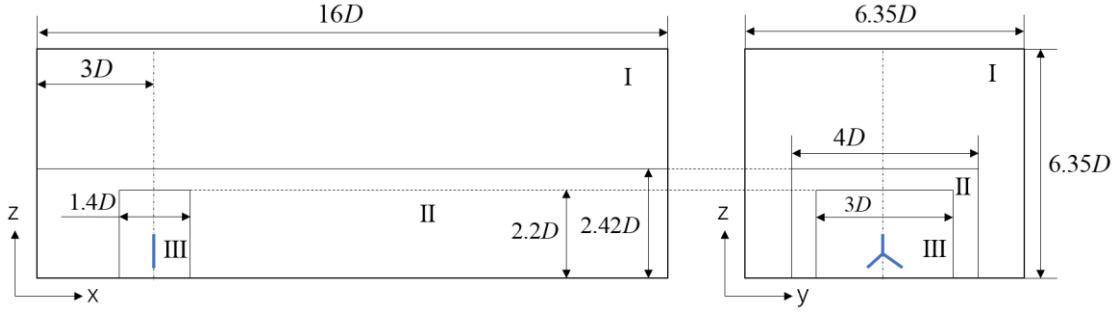

Figure 1: Layout and main dimensions of the computation domain

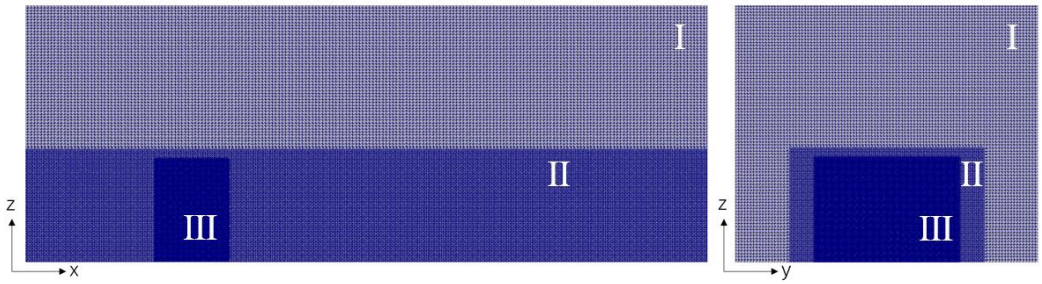

Figure 2: Mesh in lengthwise section and cross section

3.2 Boundary Condition

Three cases with different inflow conditions are set up to study the influence of different turbulent structures on the wake evolution of a NREL 5MW wind turbine[16], whose rotor diameter D and hub height H_{hub} are 126m and 90m respectively. In case 1, the uniform streamwise velocity of $U_0 = 11.4$ m/s (the rated wind speed of the NREL 5MW wind turbine) is applied to the inlet boundary, while in case 2, the inflow condition changes to a turbulent inflow of which the mean streamwise velocity still equals to U_0 but also exists a random fluctuation with a turbulence intensity equal to 10%, 2% and 2% of U_0 respectively in x, y and z dimension. In case 3, an atmospheric neutral boundary layer (NBL) flow is simulated. Different from other cases, the velocity and turbulence intensity of NBL flow cannot be directly prescribed in the inlet plane. A fully developed boundary layer flow has to be simulated in a so-called precursor case, where the data obtained in each cross section is collected and stored as the inflow database of the successor case, i.e. case 3. In cases 1 and 2, the side plane is subject to the symmetry boundary condition, which means the velocity

gradient in crosswise direction is zero, and the free-slip condition is applied to both the top and bottom planes so the friction effect of the ground is not considered. The traditional Neumann boundary condition (zero normal gradient) is imposed to the outlet of the domain. In case 3, The wall model mentioned in section 2 is applied to to simulate the effect of the rough ground. The side plane boundary condition is set to be cyclic, the same as they are in the precursor case to insure the coherence of the atmospheric turbulent structure. The boundary conditions of top and outlet planes are the same as those in case 1 and 2.

4 RESULTS AND DISCUSSIONS,

All three simulation cases last for 300s and only the flow data in the last 2 minutes are used in the following analysis, because the wake of the wind turbine needs about 3 minutes to arrive at the end of the computational domain. In this part, the neutral boundary layer flow simulated in the precursor case is firstly validated and the time averaged flow information such as velocity in streamwise and vertical dimensions and Reynolds shear stress is then provided. Finally, the finite time window filter technique is introduced to learn the wake meandering features in certain moments and different cross sections downstream.

4.1 Validation of the Simulated NBL Flow

As mentioned in part 3, a precursor case should be implemented to generate an atmospheric flow with neutral stability over flat terrain, from which the data collected are introduced to the inlet plane of case 3. The quality of the computation in precursor case has a vital influence on the simulation in the successor case. Only when the simulated atmospheric flow reaches the quasi-equilibrium, the flow information can be collected and used as the inflow data for the successor case. The precursor simulation lasts for 18,000s before data collecting and after that the flow information from 18,000s to 18,300s is used for the following analysis and the inflow condition of case 3. Because the two main characteristics of atmospheric flow that directly affect the performance of wind turbines are wind speed and turbulence intensity, the consistency of the temporal average of these two characteristics in different downstream positions is considered the sign of the quasi-equilibrium flow. Figure 3(a) shows the streamwise velocity profile in vertical dimension and the red, blue and green represents the results in 3D, 8D and 13D downstream positions respectively. Three red dotted lines mark the heights of bottom, hub and top of the rotor. The flow statistics of three positions show good agreement and reach the rated wind speed 11.4m/s at hub height 90m. The decline of the wind speed at around 750m height is caused by the prescribed capping inversion where the potential temperature gradually increases from 300K to 308K in the 100m vertical distance starting at 750m. The capping inversion restricts the growth of the boundary layer flow in the limited computational domain.

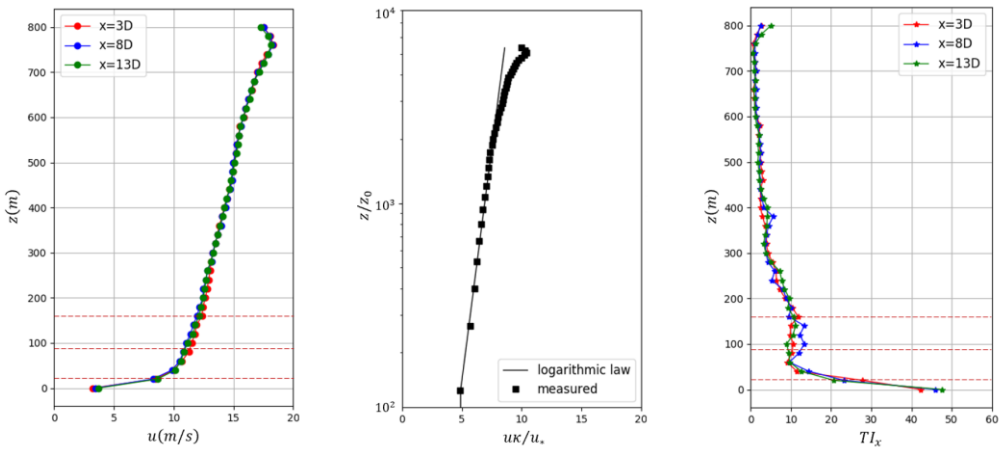

(a) Time averaged velocity profiles

(b) Normalized velocity profiles in semilog scales

(c) Streamwise turbulence intensity profiles

Figure 3: Time averaged velocity profiles and streamwise turbulence intensity profiles of the generated NBL flow in the entrance, middle and end of the domain

According to the logarithmic law of the boundary layer flow, the flow in the Prandtl layer of NBL follows the expression below:

$$\frac{\bar{u}}{u_*} = \frac{1}{\kappa}\log(\frac{z}{z_0}) \tag{9}$$

Where u_* is friction velocity and κ is Karman constant, set to 0.4 in the present study. In order to further examine the quality of the simulated NBL flow, the measured velocity profile is replotted in a semi-log coordinate system in Figure 3(b) where the logarithmic expression is also plotted as a black tilted straight solid line. The prescribed roughness length z_0 is 0.15m. Thus in this case, the dimensionless height z/z_0 of the Prandtl payer is about 1.4×10^3. As seen in the Figure 3(b), the simulated result in the Prandtl layer agrees well with the theoretical logarithmic law of the wall. The Figure 3(c) displays the profile of the streamwise turbulence intensity $TI_x = u_\sigma/\bar{u}$ (u_σ represents the standard deviation of u) in different positions. Consistency is showed again in different heights and the turbulence intensity attains around 10% in the wind turbine height. Noting that the flow information is only sampled by the probes placed in the longitudinal center plane, several inconsistent data in different downstream positions could be caused of the undetected transvers turbulent structures, which nevertheless will not have obvious influence on the evolution of the wake meandering.

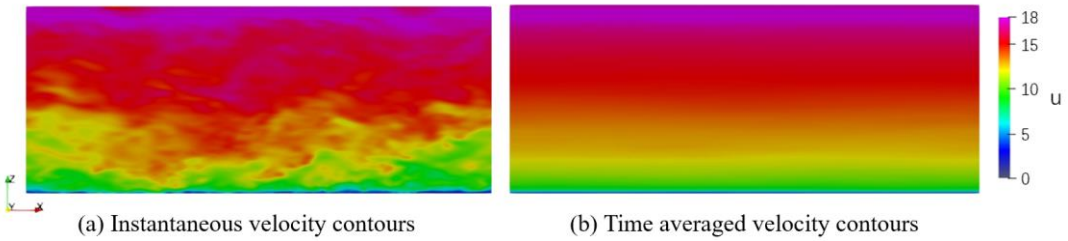

Figure 4: Streamwise velocity contours in x-z plane of an instantaneous and a time averaged flow field

Figure 4 shows the streamwise velocity contours in longitudinal center plane of an instantaneous flow field and the time averaged flow field of the precursor simulation. From the Figure 4(a), the large scale turbulent structure in atmospheric flow can be clearly distinguished and in Figure 4(b), the velocity gradient in vertical direction is stable in all streamwise position, indicating the flow has achieved a quasi-equilibrium state.

4.2 Time Averaged Wake Field

Extracting mechanic energy from the incoming flow, the wind turbine leaves a relatively low speed wake region behind the rotor, which could last for a distance up to over 10 diameters. The wind speed in the wake region will gradually recover to the velocity of the free flow as going downstream. The pace of the recovery procedure is mainly due to the turbulence characteristics of the incoming flow. The 180s~300s time averaged streamwise velocity contours in the longitudinal center plane and hub height horizontal plane of all three cases are plotted in the Figure 5. The hub, nacelle and tower are not simulated in the present work, which is the reason for the high speed tube in the center of the wake region. Comparing the velocity contours in of case 1 and case 2, similar wake evolution process can be found. This redistribution of the wake velocity could be identified by the narrowing of the high speed region behind the turbine hub. In case 2, where the streamwise turbulence intensity of the inflow reaches 20%, the dark red low velocity region behind the blades expand inside and converge in the hub center line in about 6D downstream position, while in case 1, the hub height high speed region do not disappear until 8D downstream. In case 3, although turbulence intensity is only about 10% in hub height, the exchange of the momentum in the wake is obviously much higher than that in case 2. The wind speed is redistributed much quickly and the green high speed region through the hub disappears within 2D distance downstream with the velocity deficit mostly recovered after 8D downstream.

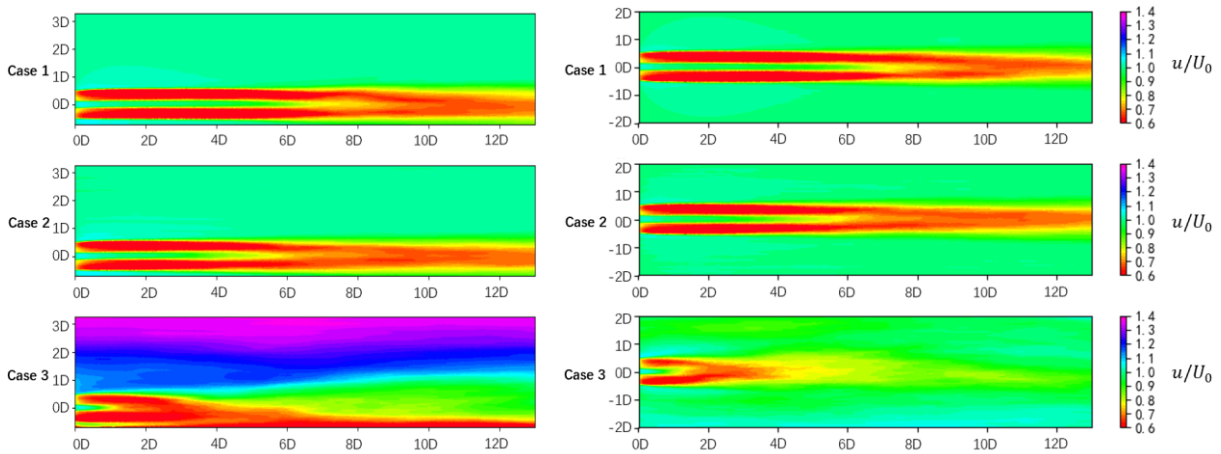

(a) Velocity contours in x-z plane (b) Velocity contours in x-y plane

Figure 5: Time averaged streamwise velocity contours in x-z and x-y planes

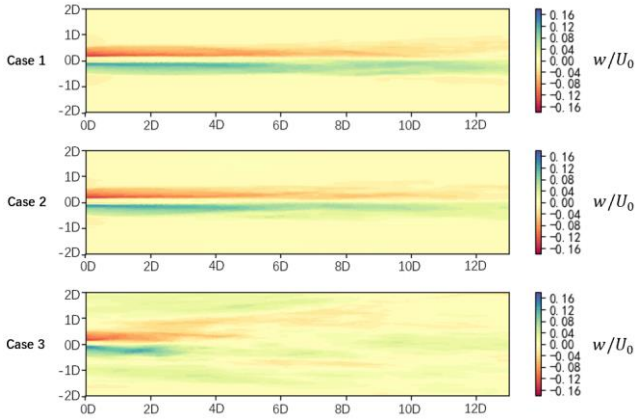

Figure 6: Time averaged vertical velocity contours in hub height horizontal plane

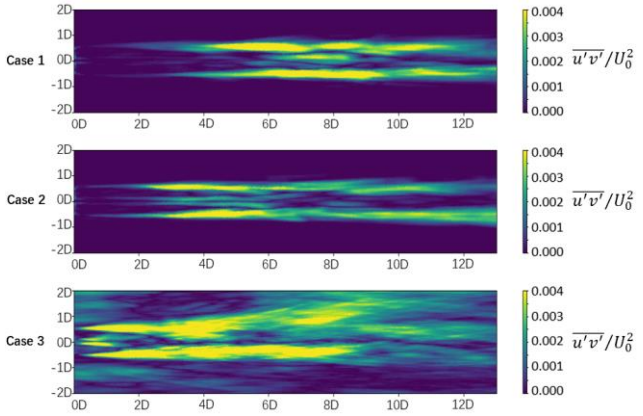

Figure 7: $\overline{u'v'}/U_0^2$ in hub height horizontal plane

Due to the conversion of the angular momentum, the wake flow rotates in the opposite direction to the rotor. As seen in Figure 6, the rotation of the wake can be clearly distinguished far away downstream from the turbine under both uniform inflow and isotropic turbulent inflow conditions, though slowed down to some degree in case 2 by the high incoming turbulence. In case 3, however, the identifiable wake rotation lasts only for a distance of 4D. This again indicates the important role of the atmospheric large scale turbulence structure in the wake evolution process. Figure 7 shows the Reynolds shear stress $\overline{u'v'}/U_0^2$ in the hub height horizontal plane, which visualizes the development of the shear layer caused by the induced vortex of the tip and root of the blades. The Reynolds stress reaches its peak where the tip and root vortex meet at the end of the near wake region. As shown in the Figure 7, under the mixing effect of the intense turbulence, the shear layers in case 2 expand rapidly and join each other 6D downstream position of the rotor, 2D distance ahead of the junction point in case 1. However, large Reynolds stress appears immediately behind the rotor in case 3, indicating the strong exchanging of the momentum in streamwise and spanwise dimension. This phenomenon explains the faster recovery of the velocity deficit under atmospheric flow condition.

4.3 Filtered Wake Field

To understand the phenomenon of the wind turbine wake meandering, a temporal filter is introduced

to ignore the small turbulent vortex and highlight the large scale movement of the whole wake. In this part, an instantaneous flow field in case 1~3 is filtered by a finite size window:

$$u_\tau(t) = \frac{1}{\tau}\int_{t-\tau/2}^{t+\tau/2} u(t')dt' \tag{10}$$

The width of the window τ is set to $0.63T \approx 3\,\mathrm{s}$, recommended in the study of Foti[19], which could conserved the coherent flow structure while smearing the high frequent turbulence. The processed flow field is presented in Figure 8, where the turbulence outside the wake region in case 2 is mostly filtered out and the large scale coherent flow structure is visible in case 3. Only in case 3 appears the large scale movement of the wake, implying that the low frequent turbulent structure in atmosphere is the main inducing factor of wake meandering phenomenon.

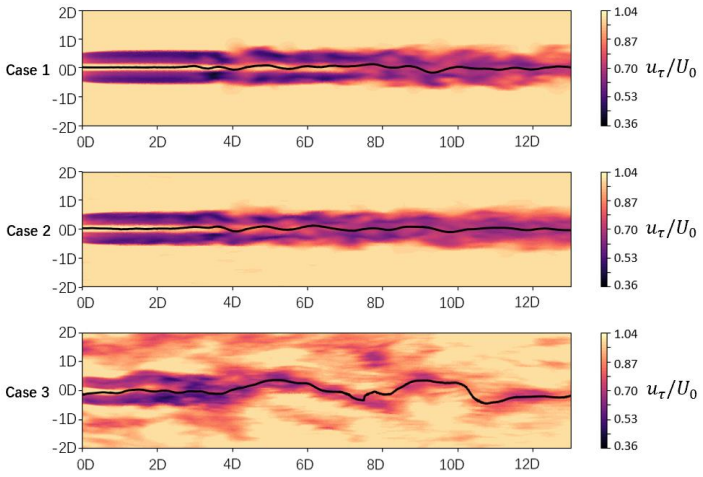

Figure 8: Contours of streamwise velocity filtered with τ-width window in hub height plane of all three cases

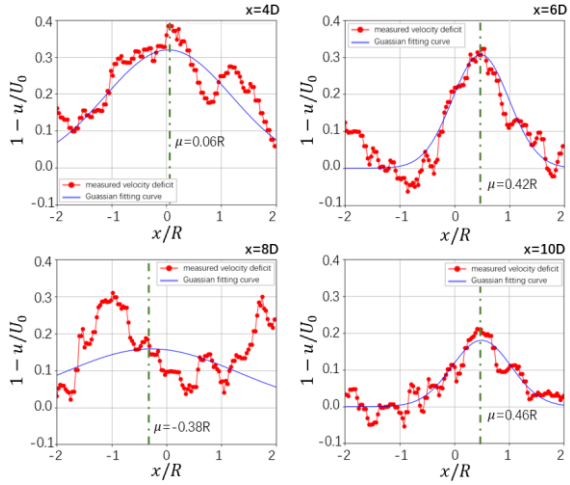

Figure 9: Gaussian fitting curves to the filtered velocity deficit in four different cross sections

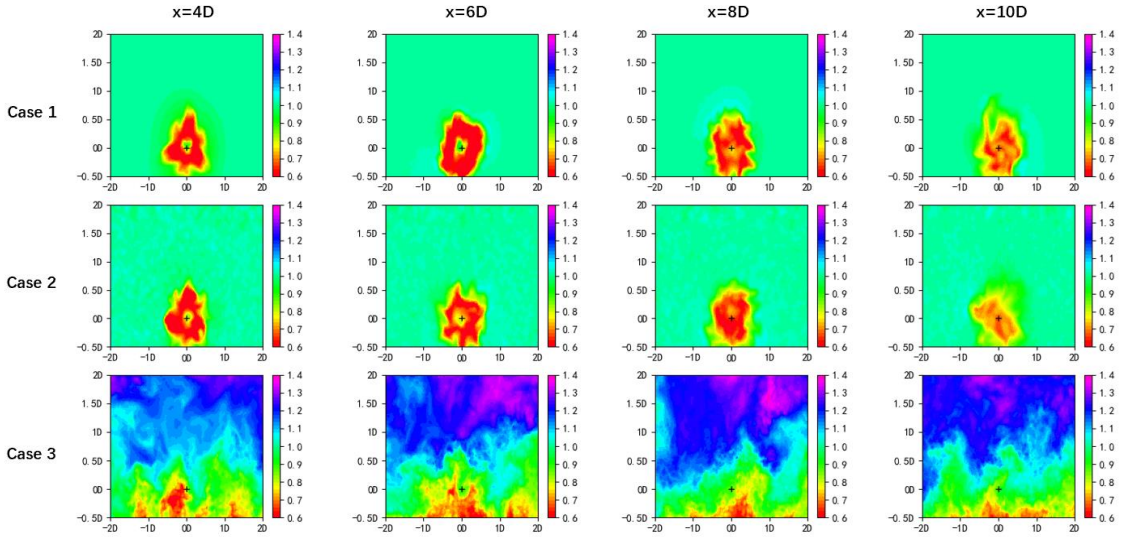

Figure 10: Contours of streamwise velocity filtered with τ-width window in different cross sections of all three cases

To further analyze the evolution of the wake, the wake center of every position downstream must be traced. Because the horizontal movement of the wake is more dominant than that in vertical direction, the present analysis is limited in the horizontal plane. There are basically three methods to locate the wake center in a cross section: 1) the maximum point of the velocity deficit 2) the weighted center of the velocity deficit

3) the μ of a gaussian curve fitted to the sampled velocity deficit data. The third is adopted in this work, considering the performance of the other two methods is more easily influenced by the original low speed air flow in the atmosphere. The fitting results in four positions downstream are displayed in Figure 9, where the wake center locations μ is marked by the green dot dash line. The Gaussian fitting curves accord well with the simulated flow in each cross section except for the 8D downstream position, where occurs a low speed air mass beside the wake, so the fitting curve compromises between the two low speed region rather than captures the wake center. This error can be avoided by narrowing the fitting range as done in the next part of the study.

Velocity contours of the filtered flow field in 4D, 6D, 8D and 10D downstream positions of three cases are also plotted in Figure 10, with the location corresponding to the rotor hub marked by a black plus sign. The shapes of the wakes in both case 1 and case 2 show similarity in each section and the wake centers stabilize around the hub center position and the velocity deficit of case 2 is less than that of case 1 in far wake region. While in case 3, the wake centers do not match the hub center but swing left and right and the edge of the wake region in 10D position cannot be clearly identified, meaning that most of the kinematic energy of the air extracted by the turbine is recovered.

4.4 Wake Meandering

In this part, the wake meandering phenomenon is studied quantificationally by analyzing the fitting data of the filtered flow field in temporal and spatial dimension. Firstly the estimated wake centers data derived from the gaussian fitting curves of every time step in each downstream position of case 1~3 are collected and the rms of horizontal deflections of the wake center from the hub center are computed and plotted in Figure 11. Under the influence of the atmospheric turbulence, the transverse movement of the wake in case 3 is much larger than those in cases 1 and 2. Moreover, the rms of the wake deflection in case 3 increases as going downstream, reaching $R/2$ in 8D downstream. More work should be done to find the precise relation between the streamwise distance and the wake deflection. Results indicates again that only the large scale turbulent structure can induce meandering of the wake.

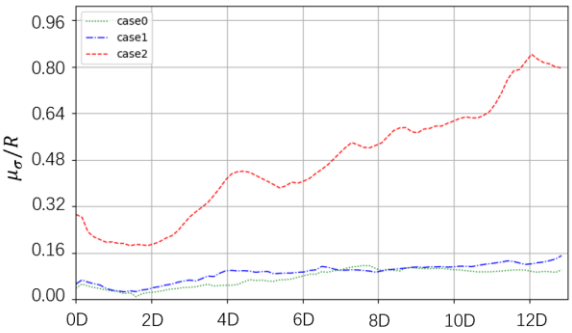

Figure 11: The standard deviation of the wake deflection μ along the x direction of all cases

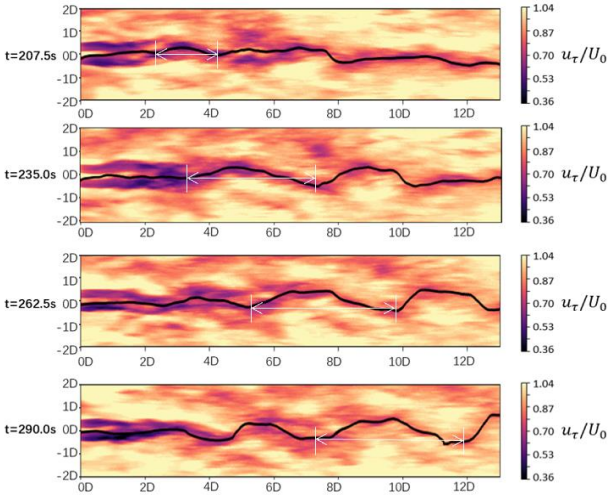

Figure 12: Streamwise velocity contours of four typical moments filtered with τ-width window in hub height plane in case 3

Velocity contours of four typical instantaneous filtered flow fields in hub height plane with wake center traced by thick black solid line are shown in Figure 12. Near wake region colorized purple, far wake region and air flow with low wind speed colorized red are clearly distinguished. The wake center line demonstrates the wave-like pattern along the streamwise direction. A wave segment marked by double sided arrow in each moment displays that the wake structure are elongated and transported downstream by the local air flow.

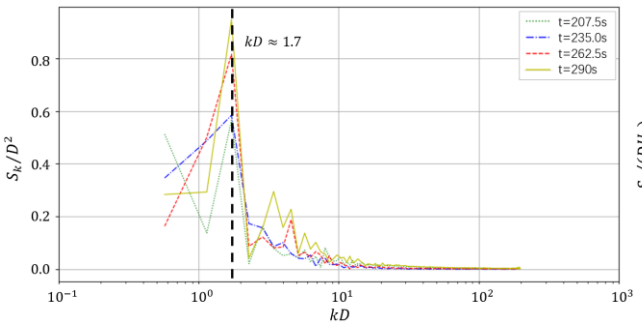

Figure 13: Spatial Fourier transformation of the wake deflection sequences of four typical moments in case 3

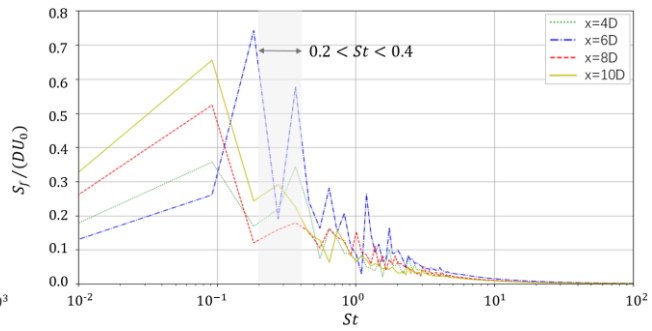

Figure 14: Power spectrum density of the velocity sequences in different downstream positions in case 3

The spatial Fourier transformation of the wake deflection sequences of the four moments in case 3 are shown in Figure 13, in which appears a mutual peak corresponding to $kD \approx 1.7$, i.e. $\lambda = 2\pi / k \approx 3.7D$. This wave length is consistent to the spacing between two extreme deflection points of the wake center line in Figure 12. In fact, the peak wave numbers of different moments could not be exactly the same value and the high consistency shown in Figure 13 is due to the limited spatial resolution of the sequences (sampling interval $\Delta x = 2$ m). The wake center represents the location with the highest velocity deficit, so the velocity fluctuation of the hub center position could, to some degree, reflect the motion of the wake. The temporal velocity sequences between 180~300s of the hub center position in 4D, 6D ,8D and 10D downstream section in case 3 are collected with a sampling frequency $f_s = 50$ Hz, and the results of the Fourier transformation is drawn in Figure 14, where the frequency in horizontal axis is nondimensionalized to Strouhal number $St = fD/U_o$. Two distinct peak are visible in each section, the first corresponding to a $St \approx 0.1$, i.e. $T = D/(StU_0) \approx 110$s and the second showing $0.2 < St < 0.4$, i.e. $28\text{s} < T < 55\text{s}$. Noting the dominant meandering wave length of $3.7D$ and the local convection speed of 8~10m/s, the second peak reflects the wake meandering phenomenon and the Strouhal number accords with the results in Medici's study[5]. The first peak of the curve is considered caused by the kilometer-scale turbulent structures in the atmosphere, of which the period attains over 100s. The similar meandering frequencies in different streamwise positions indicate that the fatigue load caused by wake meandering could not be reduced by simply enlarging the spacing between wind turbines in a wind farm.

5 CONCLUSIONS

The large eddy simulations of the wake of a single NREL 5MW wind turbine under uniform inflow, turbulent inflow and atmospheric neutral boundary layer inflow are implemented in the present study to learn the influence of the characteristics of the inflow on the evolution of the wake and meandering phenomenon. The generated NBL flow in the precursor case is firstly verified by comparing the 300 seconds time averaged wind speed data of sample points with the theoretical logarithmic law of the Prandtl boundary layer flow. The wind speed in the hub height fluctuates with a rational turbulence intensity of 10% around the prescribed rated wind speed 11.4m/s.

From the results of the time averaged flow fields of case 1~3, the incoming flow with intensive homogeneous turbulence could facilitate the development of the shear layer behind the blade tip and root, leading to a faster recovery of the velocity deficit in the wake. However, the massive exchange of the momentum and mixing of the air inside and outside the wake under NBL flow occur immediately behind the rotor, enabling the compensation of the most part of the velocity deficit in less than 8D distance. Moreover, the identifiable wake rotation in case 3 visualized by the velocity in vertical dimension disappears in 4D distance downstream, which is much earlier than in other two cases. Then the flow field is filtered by a finite time window with a width $\tau = 3s$. In this way, large scale coherent flow structure is highlighted and the wake center line in horizontal plane of case 3 shows fluctuation with an amplitude of nearly a rotor radius, but no similar phenomenon is detected in case 1 and 2. The rotation, deflection and velocity distribution of the wake in NBL are much different from those in case 1 and 2, emphasizing the importance of the study of the

atmospheric flow features in the research and industrial practice of wind energy. In the final part, the wake meandering in case 3 is further studied. The results show a continuous increment of the rms of the wake center deflection as the flow goes downstream. Because the local wind speed also increases in this process, the meandering frequency stabilizes in the same range in different position downstream, corresponding to $0.2 < St < 0.4$. Results of the spatial Fourier transformation of the wake deflection sequences also imply a dominant wave length $\lambda = 3.7D$ of the meandering wake center line.

This work emphasizes the role of the atmospheric large scale turbulent structures in inducing the wake meandering phenomenon and obtains some intrinsic physical features of the large scale movement of wind turbine wake, but systematic work should be done in the future to further study the influence of the stability of atmosphere, ground roughness length and other factors on the wake meandering and the aerodynamic performance of the downstream wind turbines.

ACKNOWLEDGEMENTS

This work is supported by the National Natural Science Foundation of China (51879159, 51490675, 11432009, 51579145), Chang Jiang Scholars Program (T2014099), Shanghai Excellent Academic Leaders Program (17XD1402300), Program for Professor of Special Appointment (Eastern Scholar) at Shanghai Institutions of Higher Learning (2013022), Innovative Special Project of Numerical Tank of Ministry of Industry and Information Technology of China (2016-23/09) and Lloyd's Register Foundation for doctoral student, to which the authors are most grateful.

REFERENCES

1. Bingöl F, Mann J, Larsen G C. Light detection and ranging measurements of wake dynamics part I: one-dimensional scanning[J]. Wind Energy, 2010, 13(1):51-61.
2. Crespo, A., Hernandez, J., & Frandsen, S. (1999). Survey of modelling methods for wind turbine wakes and wind farms. Wind Energy: An International Journal for Progress and Applications in Wind Power Conversion Technology, 2(1), 1-24.
3. Andersen, S. J., Sørensen, J. N., & Mikkelsen, R. (2013). Simulation of the inherent turbulence and wake interaction inside an infinitely long row of wind turbines. Journal of Turbulence, 14(4), 1-24.
4. Medici, D., & Alfredsson, P. H. (2006). Measurements on a wind turbine wake: 3D effects and bluff body vortex shedding. Wind Energy: An International Journal for Progress and Applications in Wind Power Conversion Technology, 9(3), 219-236.
5. Medici, D., & Alfredsson, P. H. (2008). Measurements behind model wind turbines: further evidence of wake meandering. Wind Energy: An International Journal for Progress and Applications in Wind Power Conversion Technology, 11(2), 211-217.
6. Okulov, V. L., & Sørensen, J. N. (2007). Stability of helical tip vortices in a rotor far wake. Journal of Fluid Mechanics, 576, 1-25.
7. Okulov, V. L., Naumov, I. V., Mikkelsen, R. F., Kabardin, I. K., & Sørensen, J. N. (2014). A regular Strouhal number for large-scale instability in the far wake of a rotor. Journal of Fluid Mechanics, 747, 369-380.
8. Aubrun, S., Espana, G., Loyer, S., Hayden, P., & Hancock, P. (2012). Is the actuator disc concept sufficient to model the far-wake of a wind turbine?. In Progress in Turbulence and Wind Energy IV (pp. 227-230). Springer, Berlin, Heidelberg.
9. Aubrun, S., Loyer, S., Espana, G., Hayden, P., & Hancock, P. (2011). Experimental Study on the wind turbine wake meandering with the help of a non-rotation simplified model and of a rotating model. In 49th AIAA Aerospace sciences meeting including the new horizons forum and aerospace exposition (p. 460).
10. Espana, G., Aubrun, S., Loyer, S., & Devinant, P. (2012). Wind tunnel study of the wake meandering downstream of a modelled wind turbine as an effect of large scale turbulent eddies. Journal of Wind Engineering and Industrial Aerodynamics, 101, 24-33.
11. Ivanell, S., Mikkelsen, R., Sørensen, J. N., & Henningson, D. (2010). Stability analysis of the tip vortices of a wind turbine. Wind Energy, 13(8), 705-715.
12. Troldborg, N., Sørensen, J., & Mikkelsen, R. (2009). Actuator line modeling of wind turbine wakes. Ph. D (Doctoral dissertation, thesis). Technical University of Denmark.
13. Doubrawa, P., Barthelmie, R. J., Wang, H., & Churchfield, M. J. (2017). A stochastic wind turbine wake model based on new metrics for wake characterization. Wind Energy, 20(3), 449-463.
14. Smagorinsky, J. (1963). General circulation experiments with the primitive equations: I. The basic experiment. Monthly weather review, 91(3), 99-164.

15. Sørensen, J. N., & Shen, W. Z. (2002). Numerical modeling of wind turbine wakes. Journal of fluids engineering, 124(2), 393-399.
16. Jonkman, J., Butterfield, S., Musial, W., & Scott, G. (2009). Definition of a 5-MW reference wind turbine for offshore system development NREL. Golden CO.
17. Moeng, C. H. (1984). A large-eddy-simulation model for the study of planetary boundary-layer turbulence. Journal of the Atmospheric Sciences, 41(13), 2052-2062.
18. Monin, A. S., & Obukhov, A. M. (1954). Basic laws of turbulent mixing in the surface layer of the atmosphere. Contrib. Geophys. Inst. Acad. Sci. USSR, 151(163), e187.
19. Foti, D., Yang, X., Guala, M., & Sotiropoulos, F. (2016). Wake meandering statistics of a model wind turbine: Insights gained by large eddy simulations. Physical Review Fluids, 1(4), 044407.
20. Cheng, P., Huang, Y., Wan, D.C. (2019). A numerical model for fully coupled aero-hydrodynamic analysis of floating offshore wind turbine. Ocean Engineering, 173: 183–196
21. Cheng, P., Wan, D.C. (2019). Fully Coupled Aero-Hydrodynamic Simulation of Floating Offshore Wind Turbines with Overset Grid Technology. Lecture Notes in Civil Engineering, Volume 22, K. Murali et al. (eds.), Springer Nature Singapore Pte Ltd. 2019, pp. 647-661
22. Huang, Y., Cheng, P., Wan, D.C.(2019). Numerical Analysis of a Floating Offshore Wind Turbine by Coupled Aero-Hydrodynamic Simulation. Journal of Marine Science and Application, 18(1): 82-92